Nano Energy 41 (2017) 566–572

Contents lists available at ScienceDirect

Nano Energy

journal homepage: www.elsevier.com/locate/nanoen

Full paper

Conductive-probe atomic force microscopy as a characterization tool for nanowire-based solar cells

Dmitry Mikulik[a,1], Maria Ricci[b,1], Gozde Tutuncuoglu[a], Federico Matteini[a], Jelena Vukajlovic[a], Natasa Vulic[a,c], Esther Alarcon-Llado[a,d], Anna Fontcuberta i Morral[a,*]

[a] Laboratoire des Matériaux Semiconducteurs, Institut des Matériaux, Ecole Polytechnique Fédérale de Lausanne, 1015 Lausanne, Switzerland
[b] Cavendish Laboratory, University of Cambridge, United Kingdom
[c] School of Electrical, Computer, and Energy Engineering, Arizona State University, United States
[d] Center for Nanophotonics, AMOLF, Science Park 104, 1098XG Amsterdam, Netherlands

ARTICLE INFO

Keywords:
Next generation photovoltaics
Nanowire-based solar cells
Conductive-AFM
III–V semiconductors

ABSTRACT

The photonic properties of nanowires advocate for their utilization in next generation solar cells. Compared to traditional devices, the electric scheme is transformed from a single into an ensemble of pn junctions connected in parallel. This new configuration requires new schemes for the characterization. We show how conductive-probe atomic force microscopy, C-AFM, is an essential tool for the characterization and optimization of this parallel-connected nanowire devices. With C-AFM it is possible to obtain both surface topography and local electrical characterization with nanoscale resolution. We demonstrate topography and current mapping of nanowire forests, combined with current-voltage measurements of the individual nanowire junctions from the ensemble. Our results provide discussion elements on some factors limiting the performance of a nanowire-based solar cell and thereby to provide a path for their improvement.

1. Introduction

Semiconductor nanowires (NWs) are promising for photovoltaic applications due to their superior light absorption with respect to their thin film counterparts [1–7]. The needle-like morphology of NWs is also advantageous for the extraction of the photo-generated carriers via a radial p-n junction design [8,9]. Today, experimental efficiencies of NW ensemble solar cells are still lower than the record values for planar solar cells [10–12]. Van Dam et al. recently achieved a record conversion efficiency close to 18% for 0.09 mm^2 area of InP NWs-based solar cells [13]. These devices were fabricated using nano-imprint lithography and a top-down approach, etching down nanopillars on an InP substrate with a p-n junction. This approach guarantees the uniformity in size and electrical properties within the ensemble, although it limits the devices to an axial junction configuration. Moreover, it does not provide a path to save expensive and non-abundant elements such as indium. For a more efficient utilization of resources, NWs should be obtained in a bottom-up approach and on foreign substrates [14].

One of the major challenges in bottom-up NW ensemble solar cells is achieving perfect uniformity over the whole surface area as the individual NW p-n junctions are connected in parallel. The main concern is that the electrical properties of the NW ensemble device may be limited by the lowest performing NWs of the ensemble. So far, there is no experimental evidence of how low-performing nanowire pn junctions affect a solar cell device made of a nanowire ensemble. It is thus necessary to correlate the individual electrical characteristics of single NWs with the overall device. Only in this way it is possible to progress swiftly in the technology and to determine the factors that significantly affect the performance of the NW ensemble device. So far, to obtain this information, single NWs have been first detached from the substrate and then singularly contacted to perform electrical measurements. This process requires a long nanofabrication process [15]. In addition, the NW is isolated and positioned horizontally on a substrate, thereby strongly changing the light absorption conditions [16]. Finally, the influence of the interface and band-alignment between semiconductor NW and a foreign substrate (e.g. GaAs on Si) cannot be addressed by this technique.

Conductive-probe atomic force microscopy (C-AFM) is a powerful current-sensing technique for the characterization of conductivity variations in resistive samples. C-AFM can simultaneously map surface topography and current distribution of samples by applying a constant voltage between the scanning conductive tip and the sample surface.

* Corresponding author.
E-mail address: anna.fontcuberta-morral@epfl.ch (A. Fontcuberta i Morral).
[1] These authors contributed equally to this work.

http://dx.doi.org/10.1016/j.nanoen.2017.10.016
Received 15 May 2017; Received in revised form 4 October 2017; Accepted 5 October 2017
Available online 06 October 2017

The main appeal of C-AFM is the possibility to access local conductivity information down to the nanoscale and, at the same time, to explore significantly large areas of the sample surface during the scanning process [17,18]. This enables, in the specific case of NWs forest, to have single wire resolution but on a statistically significant number of NWs. C-AFM has been widely used to characterize single NWs but without luck in terms of linking morphology and electrical properties [19–23]. The main issue in the case of standing NWs is the big roughness of the sample that makes challenging a proper tracking of the surface and thus a reliable mapping of the sample conductivity.

In this paper, we demonstrate the use of C-AFM for individually characterizing electrical properties of self-assembled GaAs NW p-n junctions standing on a doped Si substrate on which they were grown by Molecular Beam Epitaxy (MBE). In addition, we compare the obtained data from C-AFM with standard current-voltage (IV) measurements of single NW and ensemble solar cells by probe station. When operated in contact mode, the lateral-spatial resolution of C-AFM is set by the contact area between AFM tip and sample. By choosing sharp probes and appropriate scanning conditions, reliable conductivity measurements are systematically obtained and standing single NWs resolved. To limit the roughness of the sample, the NWs forest was embedded in a polymeric transparent matrix, so that only the top of NWs is reached by the AFM tip. The individual photovoltaic properties are obtained by combining the C-AFM setup with an optical fiber able to introduce external light source with calibrated power. By combining the information from topography and current maps we are able to individually address the NWs. We find that the properties of the MBE-grown NW ensembles are inhomogeneous in terms of electrical properties and that up to half of the NWs can be electrically inactive. The IV characteristics on a statistically significant number of wires are obtained. The individual properties are compared to the statistically averaged properties of the ensemble. This allows us to address the limitations of the NW ensemble device. We prove C-AFM to be a fundamental technique in the analysis of NWs ensemble solar cell structures, particularly in the case of samples obtained by self-assembly growth where more inhomogeneity in the NW properties is expected. We provide a quantitative link between the single wire and the ensemble device performance. This link is fundamental for the optimization of the fabrication process.

2. Material and methods

2.1. GaAs NW growth

In this work, radial p-i-n GaAs NWs were grown on 2-in. p-doped (111) Si substrate by MBE using self-catalysed vapor-liquid-solid method (VLS). By optimizing growth parameters and thickness of native oxide on Si substrate, self-assembled GaAs NWs were grown vertically with desired geometrical properties [24]. This method allows for the growth of large area ensembles of NWs without using lithographic processes. First, p-GaAs NWs were grown using standard growth conditions, reported in [25], with addition of Si as dopant. The same Si flux used for the doping of the core leads to a nominal doping concentration of 10^{18} cm^{-3} when calibrated with secondary ion mass spectrometry (SIMS) on (100) GaAs substrates. Next, the growth conditions were switched for the shell growth by decreasing the temperature and increasing V/III ratio. This facilitates growth on {110} side facets and intrinsic GaAs shell of the thickness of 100 nm was grown. Finally, 30 nm of n-GaAs was grown using Si as dopant [15]. The nominal doping concentration was 5×10^{18} cm^{-3} in that case. The morphology of the samples was characterized with scanning electron microscopy (SEM). Images of the samples can be found in Supplementary information (SI – Fig. S1).

2.2. NW ensemble device preparation

After growth, the NWs were embedded in a polymer matrix – polydimethylsiloxane (PDMS) or SU-8, obtaining a flexible transparent thin layer. In the case of PDMS, the as-grown sample was covered with the polymeric solution by spin coating technique. To enhance the adhesion between polymer and the NW ensemble, the curing agent to base ratio was increased from standard 10% up to 20%. Due to the high density of NWs, the PDMS solution was diluted with Hexane (1:6) to decrease the viscosity of the solution. A 3 ml drop of the mixture was placed on the sample and spun at 4000 rpm for 60 s. The sample was then cured in the oven for 2 h at 80 °C to enable the hardening of the PDMS layer. Finally the PDMS surface was etched in a SF_6 plasma for 5 min to expose the NWs tips and thus enable electrical contact. In the case of SU-8, GM1040 SU-8 photo-epoxy was spun on the as-grown sample at 1000 rpm for 45 s and cured with 1 min UV light and 5 min on a hotplate at 130 °C. After the curing, 1 min oxygen plasma etch was performed to remove SU-8 residuals from the NW tips.

Finally, the front and back contacts were fabricated, so that the radial p-i-n GaAs NW ensemble could also be used as a solar cell. Front contacts were produced by RF sputtering a transparent 200 nm thick Indium tin oxide (ITO) film at room temperature (RT) with a rate of 18 nm min^{-1} and 15 sccm of Ar and 2 sccm of O_2 gases. A 200 nm DC sputtered film of Al was used as a bottom contact to the p-doped Si substrate which was preliminary dipped in buffered HF solution to remove native oxide. To facilitate the electrical probing, a Ti/Au (10/100 nm) contact frame was electron-beam evaporated on the sample through a hard stencil mask. It is worth noting, that for C-AFM measurements, the top contact was avoided in order to eliminate any influence of the surrounding NWs on the IV measurements.

2.3. Conductive-probe atomic force microscopy

Fig. 1 shows C-AFM setup (A) and the SEM image (B) of the GaAs NW ensemble sample. The NW array has been fabricated with the same process flow as the solar cell, only the top contact is missing so that the individual IV curves can be recorded. C-AFM measurements were performed using two different AFM equipment: the ORCA module of a Cypher-S AFM and the C-AFM module of a Bruker ICON system. In the first case, we used internal light-emitted diode (LED) lamp to determine the photo-response of NWs in ensemble and analyse behaviour of NW p-i-n junctions under different applied voltage. The IV statistics of NW p-i-n junctions were collected with the Bruker ICON system. To illuminate the sample, an external light source from a quartz tungsten halogen lamp was introduced into the AFM set-up through an in-built optical microscope. Due to the internal losses inside optical system, the total light intensity was much lower than 1 sun. The exact spectrum and measured light intensity can be found in SI (Fig. S3-1). The aluminium back contact of the sample was attached to a standard metal disk with conductive epoxy glue. The electrical connection between the metallic disk and the voltage supply was obtained using the tools and procedures described by the AFM provider [26,27]. For the electrical measurements, solid Pt tips were mounted on the cantilever holder. The exact procedure of measurements and details on AFM tips are given in Supplementary information (see Fig. S3). Standard imaging (not electrical measurements) was performed in Amplitude Modulation using the same machine but with the normal cantilever holder and standard AC240TS tips.

2.4. Standard device and single NW electrical measurements

The IV measurements of the NW ensemble device were performed by contacting the samples with 2-points custom-made needle probe station, equipped with a source meter unit used as a voltage source and current meter. The series of IV measurements were obtained first in the dark and then under light illumination using a one-sun simulator. The

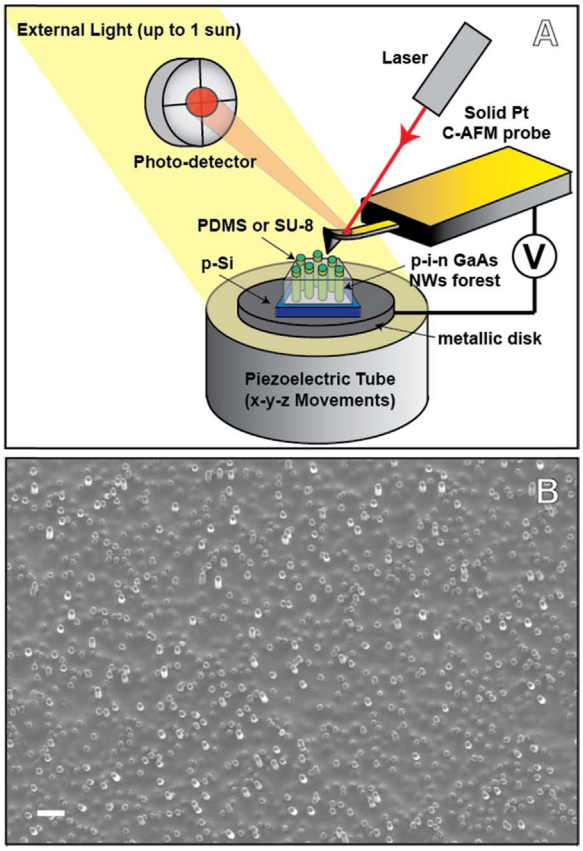

Fig. 1. Schematic illustration of C-AFM setup (A) and SEM image of GaAs NWs embedded in polymer matrix (B). The sample for C-AFM measurements is electrically connected to a metallic disk and a bias between the Pt probe and the sample is applied while scanning the surface. The piezoelectric tube enables fine movements in the three x-y-z directions. An external light source is mounted in the AFM enclosure. The light beam with a calibrated power is impinging on the sample. The scale bar is 2 μm.

intensity was calibrated with the help of a reference solar cell.

In order to validate the C-AFM method, we also provide electrical measurements of the single NW, detached from the substrate and contacted horizontally. For the contacting, we followed the procedure described by Colombo et al. [15]. Shortly, after detaching the NW p-n junctions from their native Si substrate, we transferred them on a Si wafer covered by an insulating SiO_2 layer and markers for lithography alignment. Next, e-beam lithography is used to form a contact scheme, followed by evaporation of Pd/Ti/Au (40/10/150 nm) contacts for p-type and Pd/Ge/Au (40/170/50 nm) contacts for n-type GaAs. The IV characteristics were measured both in the dark and under 1-sun (AM 1.5) illumination.

3. Results and discussion

3.1. Standard NW solar cell characterization

Prior to the C-AFM measurements and in order to have a reference of our device properties, we have characterized the NW-based solar cells in two ways: (i) ensemble device characterization by contacting the NW ensemble and (ii) single NW characterization by detaching and contacting separately from the native Si substrate [28–31]. The active surface of the measured device corresponded to 13.9 mm^2. An optical image of the ensemble device as well as an SEM image of the single NW device can be found in SI (see Figs. S2 and S4, respectively). IV measurements were performed both in the dark and under 1-sun illumination. In order to extract the ideality factor (n) and series and shunt resistances (R_s *and* R_{sh}), we fitted I–V curves using the 1-diode model (more Supplementary information in SI – Fig. S5).

Fig. 2A depicts the electrical characteristics of the NW ensemble solar cell. The open-circuit voltage (V_{oc}) of the NW ensemble device is 0.24 V, a value much smaller than those found in GaAs solar cells (thin film GaAs – 1.122 V [12], NW array – 0.923 V [32]). The short-circuit current density (J_{sc}) of 12.5 mA/cm^2 is far below the predicted maximum of 28 mA/cm^2 as well. We can calculate the average short-circuit current from each NW (I_{sc}^{nw}), which is the measured $J_{sc}^{ensemble}$ from the NW ensemble device IV divided by the number of NWs in 1 cm^2. Therefore, on average, each NW generates I_{sc}^{nw} of 25 pA, which is an order of magnitude lower than previously reported elsewhere [1]. The ideality factor of the full device is 2.56, which indicates possible tunnelling through internal barriers or additional recombination pathways at the interfaces that will be explained further.

Fig. 2B shows IV measurements of a single NW solar cell horizontally lying on an oxidized silicon substrate. The single NW solar cell and the NW ensemble device both come from a sample obtained under the same growth conditions. The active area was calculated by multiplying the NW diameter by the length of the exposed p-i-n junction, as in Ref. [15] (see Fig. S4). The obtained values for I_{sc} of 50 pA (or 18 mA/cm^2) and V_{oc} of 0.55 V are significantly higher than the estimated average values from the ensemble device measurements (25 pA and 0.24 V, respectively). In addition, the ideality factor of the single NW, n = 1.79, is much lower than in the case of the NW ensemble device. Comparing the single and ensemble devices, there is also one and two

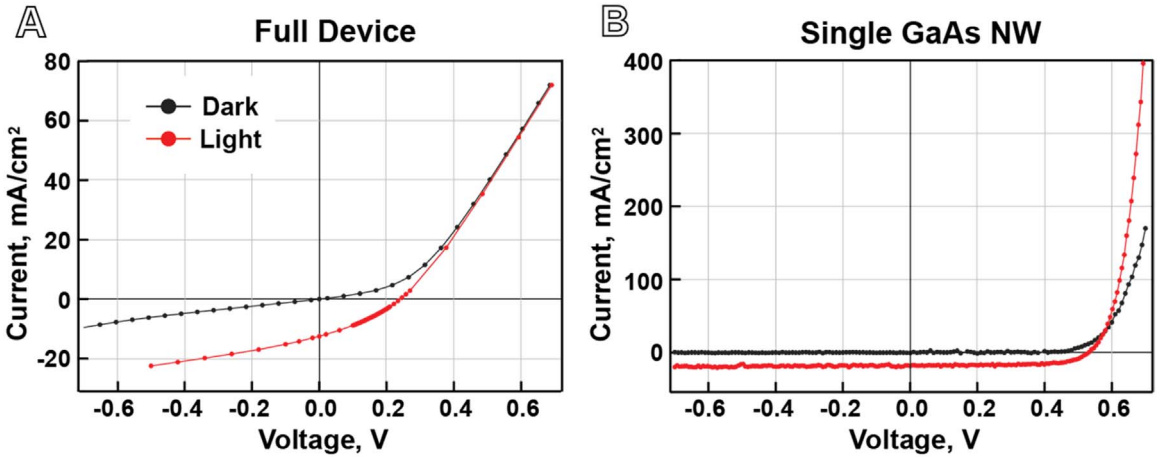

Fig. 2. NW ensemble device (A) and single NW (B) IV measurements. In both cases the measurements are performed first in the dark (black curves) and then under 1-sun illumination (red curves). The current density in the case of the ensemble device is 12.5 mA/cm^2, while for a single NW 18 mA/cm^2. Series and shunt resistances (R_s and R_{sh}) are at 4.2 and 46.9 Ω cm^2 for the ensemble device and 0.04 and 447 Ω cm^2 for a single NW.

orders of magnitude difference in R_{sh} and R_s respectively. We attribute this difference in the electrical properties to the lack of GaAs/Si heterojunction in the single NW scheme, as opposed the NW ensemble device obtained on a Si substrate and that can induce a barrier at the interface. Here below we outline in more detail the different causes of the discrepancy between single and ensemble device characteristics:

- Electrical contact configuration: in the single NW configuration ohmic contacts do not need to be transparent. As a consequence, there are less restrictions in the material choice and ohmic contacts are more easily obtained. Since in the NW ensemble configuration the top contact must be as transparent as possible, the device can suffer from increased series resistance as compared to a direct Pd-Au contact. Contacting through the substrate might also provide some additional series resistance and a hetero-barrier due to the valence band discontinuity between GaAs and Si [33].
- Dielectric environment: in the NW ensemble device we find that the polymeric matrix can eventually be charged. The electrostatic interaction with the matrix affects the electrical properties of the ensemble device, especially when compared to the single NW configuration.
- Difference in the light distribution within the NW core: the single NW is lying on the surface while NWs in the forest are standing and illuminated from above. This results in significantly different absorbance [16,34].
- Intrinsic high inhomogeneity of the NWs due to the growth process.
- Presence of the non-active NWs in the ensemble device: some of the NWs could be in an open-circuit configuration. For example, during the fabrication process, few NWs can bend and break or are partially covered by the polymer. If this is the case, the corresponding area does not contribute to the overall photocurrent.

It is challenging to understand in more depth the limitations of the system by means of the traditional characterization methods. The issue of the non-uniformity of the NWs grown by VLS method was addressed in case of GaN NW LED structures by Limbach et al. [35]. The NW-to-NW fluctuations in series resistance lead to broad range in current density between them, resulting in preventing some of the NWs to emit light. Also, in the use of NWs for photoelectrochemistry experiments, it was observed that the photovoltage of the NW array photoelectrode is highly affected by the worst-performing NW [36]. Our original approach here consists of addressing some of these issues in our devices in a more systematic way by C-AFM.

3.2. Conductive AFM: morphology and current maps

Current mapping and single NW IV measurements were performed by C-AFM. We performed measurements in the dark and under illumination by using: a) an in-built calibrated LED lamp; b) a light source from a sun simulator. The sample for AFM measurements was obtained with the same growth conditions as NW ensemble device, as described in experimental section.

3.2.1. Surface morphology and light sensitivity

We start by comparing the topographic resolution that SEM and AFM can offer (Fig. 3A and C). We then determine the number of light-responsive NWs in that area by C-AFM. For this, we measure the same area by SEM, topographic AFM and C-AFM.

To find the same area of the NW ensemble in the different set-ups, a gold grid was evaporated onto the surface (see in Supplementary information – Fig. S3-2). In Fig. 3A and C the exact same $5 \times 5\ \mu m^2$ area of the surface is presented by respectively SEM and AFM. As a reference, we highlight identical NWs with a circle and coloured arrows. From both SEM and topographic AFM it is possible to clearly recognize the wires that protrude from the surface. We count a total of 42 wires for this scanned area. Next, we performed C-AFM on the same area. With the purpose of revealing the percentage of photo-active nanowires, we illuminated the sample with a white LED while applying a zero voltage between the tip and the sample. A more precise characterization with a calibrated lamp is shown in the last part of the paper (Section 3.2.3). Fig. 3B corresponds to the 3D topography image of a GaAs NW ensemble overlaid with the current map (at 0 V under light) performed by C-AFM. The area between NWs is not conductive, being an insulating polymer. All NWs, being connected to the back contact, should ideally provide negative current (photocurrent) at zero bias and under illumination. The measurement in Fig. 3B reveals that not each NWs exhibits photocurrent and thus not all of them are working as a p-n junction in the ensemble. Strikingly, almost half of the NWs display an absence of the photo-current (see white arrow). Interestingly, there is a factor 2 difference when comparing the average photocurrent obtained with the characteristics of the NW ensemble and the functioning single NWs (25 pA vs 50 pA).

3.2.2. Scan regime – current map

Current mappings can also be performed while applying a bias between tip and sample. An example of this kind of measurements is presented in Fig. 4. Here, the same area of the sample (topographic image Fig. 4A) is scanned several times in contact mode while applying different voltages between the tip and the sample (see Fig. 4B–E). The sample was illuminated with the internal LED lamp of the system to facilitate the experiment. The colour scale in C-AFM is set so that for NWs exhibiting different IV characteristics, one observes different grey scale values. Negative values of the current correspond to the generation of a photocurrent, while positive values to the light emission conditions of the diodes [37]. This kind of measurement allows an estimation on the level of homogeneity of dozens of NWs. In addition, by changing the applied voltage a rough estimate of the open-circuit voltage of the NW ensemble device corresponding to the explored area can be obtained. For example in Fig. 4D, most of the NWs are not detected in the current map for an applied bias of 0.5 V (the position of a NW is indicated by a red circle). Still, some of them show either a positive or negative current (see for example the indicated blue and green circles in Fig. 4D).

From this set of measurements it is clear that, not only some of the NW p-n junctions are actually light sensitive, but that there is also a wide diversity in terms of electrical characteristics of the p-n junctions that work as photodiode. In particular there is not a unique value for the open circuit voltage but rather a distribution. The value measured in the ensemble device will thus be related to this distribution. In case of parallel connection of all NWs in one device, the current values of each NW are added to provide total current, but open-circuit voltage value is strongly affected by the lowest values.

In addition, analysis of the current maps at different applied voltage shows that the light passive NWs are still electrically active (at least, part of them). This result points to the existence of additional leakage channels for NW ensemble solar cell, which in turn reduces the device performance.

It is worth to note that the effect of the tip on electrical measurements under the light should be mentioned. One could expect shadowing or improvement in the light coupling due to plasmonic effects, depending on the incident wavelength. This is a much more complete study that we intend to perform in a follow-up study.

3.2.3. Single NW current-voltage measurements and ensemble properties

Unlike the previous experiments, single NW IV measurements were performed using a Bruker ICON system and introduced an external light source through the built-in optical microscope. The spectrum of the introduced light can be found in Supplementary information (see Fig. S3-1). It is worth noting that the light intensity in the C-AFM was checked for being large enough to provide a fully saturated V_{oc}. By probing the top of the single NW with the AFM tip, we can measure the individual IV curve of each p-n junction separately. In order to illustrate

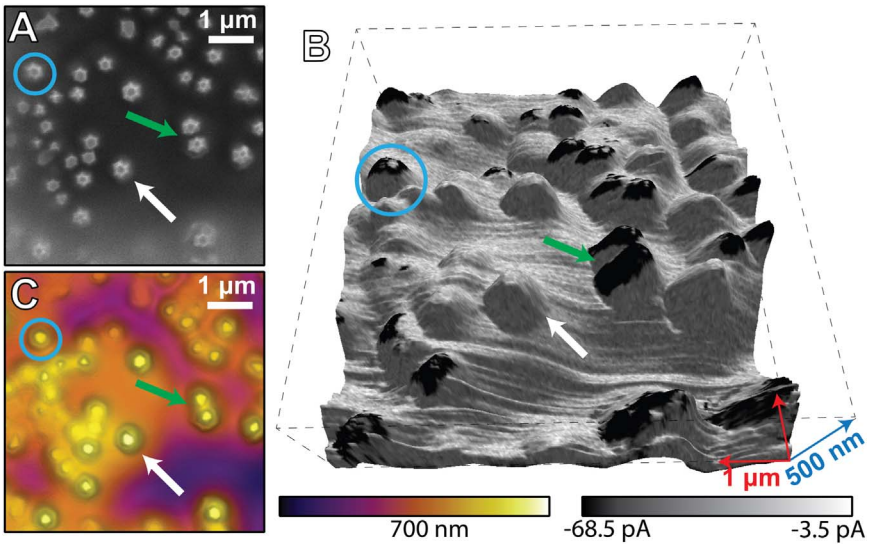

Fig. 3. SEM (A), topographic/conducting AFM (B) and topographic AFM (C) images of the same surface area of GaAs NW forest. The same NWs in the three images are highlighted by arrows and circles of the corresponding colours. Image B is obtained by superimposing to the 3D surface reconstruction of the sample the photo-current measured at 0 V between tip and sample. In B, it is clear that not all the NWs are conducting nor photosensitive at the same level. In particular, in this area, only roughly 55% of the wires are light sensitive. C-AFM image is obtained in contact mode with a Pt probe while image C is obtained with standard silicon nitride probe (see experimental section). The height scale (violet-orange-yellow) corresponds to 700 nm. The current colour scale (grey scale) ranges from −68.5 pA to −3.5 pA. AFM image was a subject to image post-processing with the Asylum research software, including optimization of the colour and scale contrast.

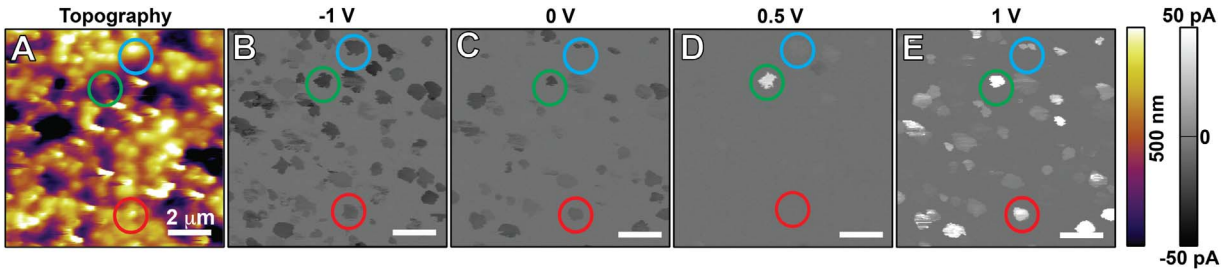

Fig. 4. Topography (A) and current maps (B-E) of GaAs NWs ensemble obtained scanning the surface in contact mode while applying different voltage between tip and sample under light illumination. The scan area is the same in all images (images are not drift corrected). The recorded current values in images B-E are presented in grey colour scale and range from −50 pA to +50 pA. Circles of different colour highlight the positions of selected NW in different images. At approximately 0.5 V of bias, most of the NWs do not conduct significantly, although few deviate from the general trend (see for example blue and green circles in D). This reflects the intrinsic inhomogeneity of the electrical properties of the GaAs NWs and the fact that the V_{oc} is unique to each NW. Height data scale range (Violet-orange-yellow colour scale) corresponds to 500 nm.

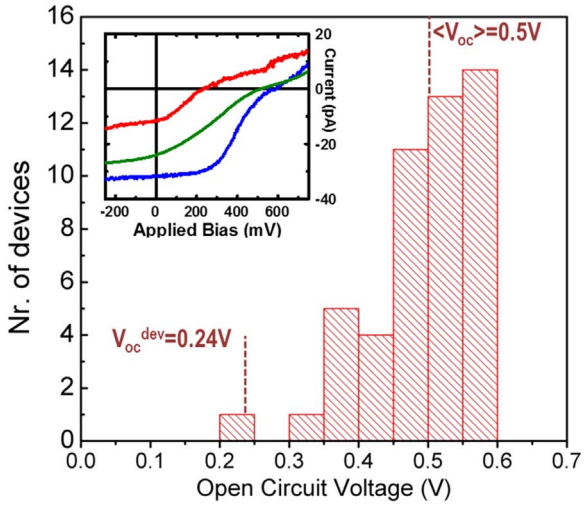

Fig. 5. V_{oc} statistics of ensemble of NWs by C-AFM. The calculated combined V_{oc} of the NWs connected in parallel ($< V_{oc} >$) and the V_{oc} of the NW ensemble device (V_{oc}^{dev}) are marked on the graph by vertical lines. The inset shows 3 IV curves under the light – the worst performing NW junction (red) and the best performing NW junction (blue) from the obtained statistics plus the calculated total IV of the virtual device (green) with the average current (total current divided by 50, the number of NW devices).

the inhomogeneity in the sample, we extracted the IV curves from 50 NW p-i-n junctions over 4 surface areas of 5 × 5 μm^2 found in the same sample as shown in Figs. 3 and 4. In Fig. 5, the V_{oc} distribution is shown and it ranges from 0.25 to 0.6 V. While most of the p-i-n junctions provide a high V_{oc} around 0.5 V, a very small number of junctions underperforms with V_{oc} values as low as 0.25 V.

While one may think that a NW p-i-n junction with a small V_{oc} may underpin the overall V_{oc} of the device, its contribution may become insignificant. The V_{oc} corresponds to the voltage at which the total current of the device is null, and in a parallel-connection configuration it can be described as:

$$\sum_{i=1}^{n} \boldsymbol{I_i}(\boldsymbol{V} = \boldsymbol{V_{oc}}) = \mathbf{0}$$

where n – is the number of NWs, and $\boldsymbol{I_i}$ – current of i-NW at V = V_{oc}. This equation highlights the importance of the ensemble measurements and the impact of an underperforming NW junction.

In the inset of Fig. 5, we show examples of IV characteristics of two individual junctions from our statistical sample along with the calculated output of what would be a device with all the 50 junctions connected in parallel (more details in Supplementary information – Fig. S6). Strikingly, the overall performance is not as dramatically affected by the underperforming junction as one may initially expect. The reason relies on the shape of the individual IV characteristics. In particular, we observe a large series resistance in the individual cells that improves with illumination intensity (see curves under different illumination conditions in Supplementary information – Fig. S3-3). This most probably comes from the p-doped core and the presence of a barrier at the GaAs/Si hetero-interface. This heterobarrier is also reflected by the large ideality factor of 5.96. We plan to further investigate the role of the interface between GaAs NWs and the Si substrate as it can seriously affect the integration of III–V solar cells on Si.

Thanks to the large series resistance, the rise in current at forward bias (i.e. $V > V_{oc}$) is not as sharp as in ideal diodes. As a consequence, the small number of poor performing junctions is being able to easily compensate for the photocurrent of the other individual parallel junctions.

We have calculated the effective open circuit voltage of the combined IV characteristics of the 50 NW devices. We obtain $< V_{oc} > =$ 0.5 V for the area investigated with the C-AFM. This value is much higher than one obtained in the NW ensemble device (0.24 V). We believe that this discrepancy is to the due to small number of NWs with low V_{oc} for the investigated areas and the large series resistance coming from the tip contact and the lower illumination intensity. In addition, it is possible that the NW ensemble device also exhibits losses from a non-optimized fabrication process such as leakages around the edges and through the non-photoactive NWs, which could also limit the performance of NW ensemble solar cells. In any case, the C-AFM technique allows us to identify high quality areas that could derive in highly performing devices. Since C-AFM is non-destructive method and can be applied directly before the fabrication of the top transparent contacts.

4. Conclusions

In conclusion, we have demonstrated the use of C-AFM to characterize the individual electrical properties of nanowire p-i-n junctions in an ensemble solar cell device. We obtained the statistical characteristics and a quantified measure of the inhomogeneity spread in the large ensemble. Our method provides the link between the individual NW and the NW ensemble solar cell performance and the importance of homogeneity in the overall device performance. We also show that few poor-performing single NWs may not have a dramatic effect on the ensemble device characteristics, but rather localized leakage paths. By comparing IV curves of NWs connected to or detached from the substrate, we outlined the influence of the interface barrier between GaAs NWs and the Si substrate, as well as the top transparent contacts. These results indicate some of the drawbacks of using self-assembly growth approaches for solar cells. Optimizing fabrication process and quality of the NWs in the ensemble is the path towards utilizing this technology in terrestrial photovoltaics, and C-AFM a valuable non-destructive tool towards this accomplishment.

Acknowledgements

We would like to thank NanoTera (20NA21_150950) for funding through project Synergia, ERC (239743) for the funding of the StG 'UpCon' and H2020 ITN project Indeed. JB Leran and H Potts are also acknowledged for technical support in the MBE machine. M.R. acknowledges the Swiss National Science Foundation (PZENP2_154283) for the funding of the Early Postdoc. Mobility fellowship. N.V. acknowledges the Swiss Government Excellence Scholarship. EAL acknowledges the support from the SNF Ambizione Energy program and the research program of FOM, which is financially supported by The Netherlands Organization for Scientific Research (NWO) (LMPV).

Appendix A. Supplementary information

Supplementary data associated with this article can be found in the online version at http://dx.doi.org/10.1016/j.nanoen.2017.10.016.

References

[1] P. Krogstrup, H. Ingerslev Jørgensen, M. Heiss, O. Demichel, J.V. Holm, M. Aagesen, J. Nygard, A. Fontcuberta i Morral, Single-nanowire solar cells beyond the Shockley–Queisser limit, Nat. Photonics 7 (2013) 306–310.
[2] A. Hochbaum, P. Yang, Semiconductor nanowires for energy conversion, Chem. Rev. 110 (2010) 527–546.
[3] E. Garnett, P. Yang, Light trapping in silicon nanowire solar cells, Nano Lett. 10 (2010) 1082–1087.
[4] J. Wallentin, N. Anttu, D. Asoli, M. Huffman, I. Aberg, M.H. Magnusson, G. Siefer, P. Fuss-Kailuweit, F. Dimroth, B. Witzigmann, H.Q. Xu, L. Samuelson, K. Deppert, M.T. Borgström, InP nanowire array solar cells achieving 13.8% efficiency by exceeding the ray optics limit, Science 339 (2013) 1057–1060.
[5] M.D. Kelzenberg, S.W. Boettcher, J.A. Petykiewicz, D.B. Turner-Evans, M.C. Putnam, E.L. Warren, J.M. Spurgeon, R.M. Briggs, N.S. Lewis, H.A. Atwater, Enhanced absorption and carrier collection in Si wire arrays for photovoltaic applications, Nat. Mater. 9 (2010) 239–244.
[6] S.A. Mann, S.Z. Oener, A. Cavalli, J.E.M. Haverkort, E.P.A.M. Bakkers, E.C. Garnett, Quantifying losses and thermodynamics limits in nanophotonic solar cells, Nat. Nanotechnol. 11 (2016) 1071–1075.
[7] A. Standing, S. Assali, L. Gao, M.A. Verheijen, D. van Dam, Y. Cui, P.H.L. Notten, J.E.M. Haverkort, E.P.A.M. Bakkers, Efficient water reduction with gallium phosphide nanowires, Nat. Commun. 6 (2015) 7824.
[8] M. Kayes, H.A. Atwater, N.S. Lewis, Comparison of the device physics principles of planar and radial p-n junction nanorod solar cells, J. Appl. Phys. 97 (2005) 114302.
[9] R.R. LaPierre, A.C.E. Chia, S.J. Gibson, C.M. Haapamaki, J. Boulanger, R. Yee, P. Kuyanov, J. Zhang, N. Tajik, N. Jewell, K.M.A. Rahman, III–V nanowire photovoltaics: review of design for high efficiency, Phys. Status Solidi – RRL 7 (2013) 815–830.
[10] G. Mariani, A.C. Scofield, C.-H. Hung, D.L. Huffaker, GaAs nanopillar-array solar cells employing in situ surface passivation, Nat. Commun. 4 (2013) 1497.
[11] M. Yao, N. Huang, S. Cong, C.Y. Chi, M.A. Seyedi, Y.T. Lin, Y. Cao, M.L. Povinelli, P.D. Dapkus, C. Zhou, GaAs nanowire array solar cells with axial p–i–n junctions, Nano Lett. 14 (2014) 3293–3303.
[12] B.M. Kayes, H. Nie, R. Twist, S.G. Spruytte, F. Reinhardt, I.C. Kizilyalli, G.S. Higashi, 27.6% conversion efficiency, a new record for single-junction solar cells under 1 sun illumination, in: Proceedings of the 37th IEEE Photovoltaic Specialists Conference, 2011, pp. 000004–000008.
[13] D. van Dam, N.J.J. van Hoof, Y. Cui, P.J. van Veldhoven, E.P.A.M. Bakkers, J. Gómez Rivas, J.E.M. Haverkort, High-efficiency nanowire solar cells with omnidirectionally enhanced absorption due to self-aligned indium–tin–oxide mie scatterers, ACS Nano 10 (2016) 11414–11419.
[14] W. Lu, C.M. Lieber, Nanoelectronics from the bottom up, Nat. Mater. 6 (2007) 841–850.
[15] C. Colombo, M. Heiß, M. Grätzel, A. Fontcuberta i Morral, Gallium arsenide p-i-n radial structures for photovoltaic applications, Appl. Phys. Lett. 94 (2009) 173108.
[16] M. Heiss, A. Fontcuberta i Morral, Fundamental limits in the external quantum efficiency of single nanowire solar cells, Appl. Phys. Lett. 99 (2011) 263102.
[17] M. Salmeron, G. Neubauer, A. Folch, M. Tomitori, D.F. Ogletree, P. Sautet, Viscoelastic and electrical properties of self-assembled monolayers on gold (111) films, Langmuir 9 (1993) 3600–3611.
[18] F. Houzé, R. Meyer, O. Schneegans, L. Boyer, Imaging the local electrical properties of metal surfaces by atomic force microscopy with conducting probes, Appl. Phys. Lett. 69 (1996) 1975–1977.
[19] S.G. Ihn, J.I. Song, T.W. Kim, D.S. Leem, T. Lee, S.G. Lee, E.K. Koh, K. Song, Morphology- and orientation-controlled gallium arsenide nanowires on silicon substrates, Nano Lett. 7 (2007) 39–44.
[20] J.S. Hwang, M.C. Kao, J.M. Shiu, C.N. Fan, S.C. Ye, W.S. Yu, H.M. Lin, T.Y. Lin, S. Chattopadhyay, L.-C. Chen, K.H. Chen, Photocurrent mapping in high-efficiency radial p–n junction silicon nanowire solar cells using atomic force microscopy, J. Phys. Chem. C 115 (2011) 21981–21986.
[21] J. Alvarez, I. Ngo, M.E. Gueunier-Farret, J.P. Kleider, L. Yu, P.R. Cabarrocas, S. Perraud, E. Rouvière, C. Celle, C. Mouchet, J.-P. Simonato, Conductive-probe atomic force microscopy characterization of silicon nanowire, Nanoscale Res. Lett. 6 (2011) 110.
[22] S. Wu, Y.M. Shao, T.X. Nie, L. Xu, Z.M. Jiang, X.J. Yang, Fabrication of straight silicon nanowires and their conductive properties, Nanoscale Res. Lett. 10 (2015) 325.
[23] F. Schuster, M. Hetzl, S. Weiszer, M. Wolfer, H. Kato, C.E. Nebel, J.A. Garrido, M. Stutzmann, Optoelectronic properties of p-diamond/n-GaN nanowire heterojunctions, J. Appl. Phys. 118 (2015) 154303.
[24] F. Matteini, G. Tütüncüoglu, H. Potts, F. Jabeen, A. Fontcuberta i Morral, Wetting of Ga on SiOx and its impact on GaAs nanowire growth, Cryst. Growth Des. 15 (2015) 3105–3109.
[25] J. Dufouleur, C. Colombo, T. Garma, B. Ketterer, E. Uccelli, M. Nicotra, A. Fontcuberta i Morral, P-doping mechanisms in catalyst-free gallium arsenide nanowires, Nano Lett. 10 (2010) 1734–1740.
[26] Asylum Research, Cypher S, 2016. ⟨http://www.asylumresearch.com/Products/Cypher/Cypher.shtml⟩. (Accessed 14 March 2017).
[27] Bruker, Dimension Icon, 2017. ⟨http://www.bruker.com/products/surface-and-dimensional-analysis/atomic-force-microscopes/dimension-icon/overview.html⟩. (Accessed 14 March 2017).
[28] M.D. Kelzenberg, D.B. Turner-Evans, B.M. Kayes, M.A. Filler, M.C. Putnam, N.S. Lewis, H.A. Atwater, Photovoltaic measurements in single-nanowire silicon solar cells, Nano Lett. 8 (2008) 710–714.
[29] J.V. Holm, H.I. Jørgensen, P. Krogstrup, J. Nygård, H. Liu, M. Aagesen, Surface-passivated GaAsP single-nanowire solar cells exceeding 10% efficiency grown on silicon, Nat. Commun. 4 (2013) 1498.
[30] E.C. Garnett, M.L. Brongersma, Y. Cui, M.D. McGehee, Nanowire solar cells, Annu. Rev. Mater. Res. 41 (2011) 269–295.
[31] A. Dalmau Mallorqui, F.M. Epple, D. Fan, O. Demichel, A. Fontcuberta i Morral, Effect of the p-n junction engineering on Si microwire-array solar cells, Phys. Status Solidi A 209 (2012) 1588–1591.
[32] I. Aberg, G. Vescovi, D. Asoli, U. Naseem, J.P. Gilboy, C. Sundvall, A. Dahlgren, K.E. Svensson, N. Anttu, M.T. Bjork, L. Samuelson, A GaAs nanowire array solar cell

with 15.3% efficiency at 1 sun, IEEE J. Photovolt. 6 (2016) 185–190.
[33] K. Tanabe, K. Watanabe, Y. Arakawa, III-V/Si hybrid photonic devices by direct fusion bonding, Sci. Rep. 2 (2012) 349.
[34] M. Heiss, E. Russo-Averchi, A. Dalmau-Mallorquí, G. Tütüncüoğlu, F. Matteini, D. Rüffer, S. Conesa-Boj, O. Demichel, E. Alarcon-Lladó, A. Fontcuberta i Morral, III–V nanowire arrays: growth and light interaction, Nanotechnology 25 (2014) 014015.
[35] F. Limbach, C. Hauswald, J. Lähnemann, M. Wölz, O. Brandt, A. Trampert, M. Hanke, U. Jahn, R. Calarco, L. Geelhaar, H. Riechert, Current path in light emitting diodes based on nanowire ensembles, Nanotechnology 23 (2012) 465301.
[36] Y. Su, C. Liu, S. Brittman, J. Tang, A. Fu, N. Kornienko, Q. Kong, P. Yang, Single-nanowire photoelectrochemistry, Nat. Nanotechnol. 11 (2016) 609–612.
[37] M. Grundmann, The Physics of Semiconductors, Second ed., Springer-Verlag, Berlin Heidelberg, 2010.